

Investigating the Center-to-Limb Effects in Helioseismic Data Using 3D Radiative Hydrodynamic Simulations

IRINA. N. KITIASHVILI  ¹

¹ Computational Physics Branch, NASA Advanced Supercomputing Division, NASA Ames Research Center
 Moffett Field, Building N-258, MS-258-6, Mountain View, CA 94035, USA

ABSTRACT

Full-disk observations from missions such as the SDO and SOHO have enabled comprehensive studies of solar oscillations and dynamics. Interpreting helioseismic and photospheric data is complicated by systematic center-to-limb variations. To explore the physical origin of these variations, we perform local 3D radiative hydrodynamic simulations that include effects of solar rotation to generate 24-hour synthetic time series of continuum intensity and Doppler velocity for nine viewing angles spanning from -75° to 75° . The simulations reveal a systematic decrease in oscillation power toward the limbs and a pronounced East–West asymmetry that increases with frequency, primarily due to rotation-induced flows. With increasing angular distance from the disk center, the amplitudes and widths of the surface gravity (f) and resonant pressure (p) modes decrease. In contrast, the amplitudes of the corresponding pseudo-modes with frequencies above the acoustic cut-off frequency increase in the intensity power spectra but are suppressed in the velocity spectra. The local helioseismology ring-diagram analysis of the simulation data further demonstrates anisotropic broadening of the modes and distinct differences in background noise and pseudo-mode structure between the intensity and velocity data. These results indicate that the center-to-limb effects arise from both geometric projection and physical factors such as line-formation height and potential effects of the radial differential rotation. The findings provide a framework for correcting helioseismic observations and demonstrate that realistic 3D radiative hydrodynamic simulations are a powerful tool for disentangling geometric and physical biases in solar data.

Keywords: The Sun (1693) — Solar physics (1476) — Helioseismology (709) — Solar interior (1500) — Solar oscillations (1515) — Solar surface (1527) — Solar atmosphere(1477) — Radiative transfer(1335) — Hydrodynamical simulations (767)

1. INTRODUCTION

To understand and build a reliable forecast of global solar activity and its evolution at different scales, it is essential to monitor the dynamics of the solar interior. There are two major approaches to probing subsurface flows. The first one is based on the analysis of surface flow properties (e.g., [Ulrich et al. 2023](#)) or tracking various features (e.g., magnetic elements, supergranulation). These types of studies rely on the direct coupling of surface and subsurface layers. For instance, such techniques are actively used to measure meridional flows and differential rotation at the photosphere by tracking small-scale magnetic elements or granulation ([Lamb 2017](#); [Roudier et al. 2018](#); [Hathaway et al. 2022](#)). The alternative approach, known as helioseismology, suggests using acoustic waves to probe the solar interior. The waves are excited below the photosphere due to the dynamics of vortex tubes and turbulence (e.g., [Unno & Kato 1962](#); [Stein 1967](#); [Kitiashvili et al. 2011, 2019](#)) and propagate through the solar interior. Changes in thermodynamic properties and flows affect oscillation frequencies and acoustic travel times, allowing us to infer these changes from the surface to the bottom of the convection zone and below. For a comprehensive overview of methods and the mathematical background, we refer the reader to the review papers by [Christensen-Dalsgaard \(2002\)](#) and [Kosovichev \(2011\)](#). Different helioseismic methods have been used to study various phenomena on a wide range of scales: from local, such as emergence and evolution of active regions (e.g., [Zhao et al. 2010](#); [Ilonidis et al. 2011](#); [Kosovichev &](#)

Duvall 2006; Stefan & Kosovichev 2023), to global, such as torsional oscillations (e.g., Howe 2020; Komm 2021). For the most recent advances in the field, we recommend the community review paper by Kosovichev et al. (2025).

Because our understanding of the solar interior relies on photospheric observations that require extensive data processing and assumptions, numerical modeling is essential for validating helioseismic inference methods and assessing their uncertainties and limitations. In particular, recent developments in 3D acoustic codes have enabled bridging the gap between global anelastic models, which are used to assess the capabilities of different global helioseismology techniques (e.g. Stejko et al. 2021, 2022; Stefan et al. 2025). The current state of the art in improving local helioseismology analysis involves using 3D realistic radiative models that can reproduce the dynamics of the Sun’s near-surface layers with great detail. For instance, this type of model has been used to investigate observational artifacts, such as the ‘concave Sun’ effect in helioseismology (Kitiashvili et al. 2015), to validate inferences of subsurface flows from time-distance helioseismology (Georgobiani et al. 2007; Zhao et al. 2007; Böning et al. 2021), to interpret the observational center-to-limb studies (Waidele et al. 2023), to test horizontal magnetic field inferences below the photosphere (Stefan & Kosovichev 2022), and others.

The center-to-limb effects in solar observations have been studied by many authors, for example, the wavelength increase of spectral lines observed closer to the solar limb relative to the disc center and foreshortening effects (e.g., Adams 1910; Evershed 1931, 1936; Higgs 1960; Howard & Harvey 1970; Stenflo 2015; Zhao et al. 2016). Also, it is well known that spectral line properties (e.g., line depth, width, asymmetry, bisector shape) vary with distance from the disk center, complicating the interpretation of observational data. In particular, helioseismic inversions can expose anomalies such as the ‘concave’ or ‘shrinking’ Sun (Duvall & Hanasoge 2009; Zhao et al. 2012), which can be reproduced through modeling of the center-to-limb variations (Kitiashvili et al. 2015). Investigating the impact of center-to-limb-related variations on observations and developing approaches to mitigate or eliminate them are primary objectives of many studies (e.g., Zhao et al. 2016; Kashyap & Hanasoge 2025). In particular, the center-to-limb effect introduces significant systematic errors in helioseismic inferences of the meridional circulation due to the strong frequency dependence of travel-time and phase shifts (Chen & Zhao 2018). Also, the ring-diagram analysis (Hill 1988) shows systematic errors for observations at off-central meridian longitudes, as well as East-West symmetry in the gradient of the solar rotation (Rabello Soares et al. 2024). Taking into account the high interest in developing forecasting techniques based on properties of the solar oscillations, e.g., to predict transient events, such as the emergence of magnetic flux with the following formation of active regions (e.g., Ilonidis et al. 2011; Stefan & Kosovichev 2023; Kasapis et al. 2025), it is essential to characterize the impact of the center-to-limb variations on helioseismic observations.

In this paper, we investigate the influence of the center-to-limb effect on oscillation power spectra in the presence of solar rotation in the quiet-Sun conditions. To perform the analysis, we run 3D radiative hydrodynamic simulations of the upper solar convection zone and the low atmosphere. Using the simulation results and a radiative transfer code, we synthesize the 6173 Å line observed by the Helioseismic and Magnetic Imager (HMI; Scherrer et al. 2012) on board the Solar Dynamics Observatory (Pesnell et al. 2012) and calculate the HMI observables (Couvidat et al. 2012): the Doppler velocity and continuum intensity. These synthetic data are then used to calculate the oscillation power spectra.

Previously, 3D realistic-type models were primarily used for testing time-distance helioseismology (e.g., Georgobiani et al. 2007; Zhao et al. 2007). Our analysis aims to investigate changes in the oscillation properties of the continuum intensity and Doppler velocity due to center-to-limb effects, focusing on the 3D power spectra used in the ring-diagram analysis. Using the identical simulation data to construct synthetic observables at various disk locations allows us to isolate and investigate the center-to-limb effect, which is not possible in observations. We first provide a brief description of the numerical model setup, spectral line synthesis, and Doppler velocity and intensity calculations, and discuss the center-to-limb properties revealed in the synthetic observables (Section 2). Section 4 describes properties of the surface gravity (f) and pressure resonant (p) modes as well as pseudo-modes (interference peaks above the acoustic cutoff frequency) presented in the oscillation power spectra as a function of the angular degree of spherical harmonics and frequency ($\ell - \nu$ diagrams). Then, we discuss properties of the 3D power spectra (the ring diagrams) at different longitudes (Section 5). In the final Section 6, we summarize our results and discuss their possible applications.

2. GENERATION OF SYNTHETIC OBSERVABLES AND MODE DEFINITION

In this paper, we used our previous 3D radiative hydrodynamic simulations of the upper convection zone and the low atmosphere, which revealed the formation of radial differential rotation, meridional flows, and a leptocline (Kitiashvili

et al. 2023). The simulations were obtained using the **StellarBox** code (Wray et al. 2018), which enables the modeling of solar convection properties and dynamics with high realism. The computational domain of the model is a rectangular box 80 Mm wide and 26 Mm deep (including 1 Mm of the atmosphere). The grid spacing is 100 km in the horizontal direction and extends vertically from 25 km at the photosphere to 82 km at the bottom of the computational domain. Thus, the overall mesh size is $800 \times 800 \times 400$ (nx×ny×nz). The solar rotation is implemented using the f-plane approximation in the rotational frame, with a rotational period of 27 days at 30° latitude (Kitiashvili et al. 2023).

In the analysis, we use a 24-hour-long time series of simulations with a 45-second cadence to synthesize the operational 6173Å(Fe I) line of the HMI Instrument. The line synthesis has been performed using the **Spinor** radiative transfer code (Frutiger et al. 2000) for the reference wavelength of $\lambda_0 = 6173.3$ Å, a range ± 0.4 Å with spectral resolution of $\lambda/\Delta\lambda \sim 3 \times 10^6$ Å. The line synthesis was performed for nine distances from the central meridian: $\pm 75^\circ$, $\pm 60^\circ$, $\pm 45^\circ$, $\pm 30^\circ$, and 0° (disk center). Since simulations are performed in the rotating frame, synthetic observables correspond to tracking the observed area with the rotation rate. In this work, we use the resulting 2D time series of the continuum intensity (I_c) and the Doppler velocity (V_D). For the continuum intensity calculations, we employ the wavelength $\lambda_c = 6172.9$ Å, which is outside of the reference Fe I line. The Doppler velocity has been computed with the center-of-gravity method

$$V_D = c * \frac{\Delta\lambda}{\lambda_0}, \quad \Delta\lambda = \frac{\sum I_i \lambda_i}{\sum I_i} - \lambda_0, \quad (1)$$

where c is the speed of light, I_i and I is the intensity at the wavelength λ_i .

We consider two types of resonance modes: acoustic or pressure (p) modes, which are trapped inside the Sun, and surface gravity or fundamental (f) modes. The modes are primarily excited by turbulent motions of the solar plasma, which excite the pressure (p -modes) oscillations through both entropy fluctuations and Reynolds stresses (Stein 1967; Goldreich & Kumar 1988) and localized events often associated with dynamics of vortex tubes in the intergranular

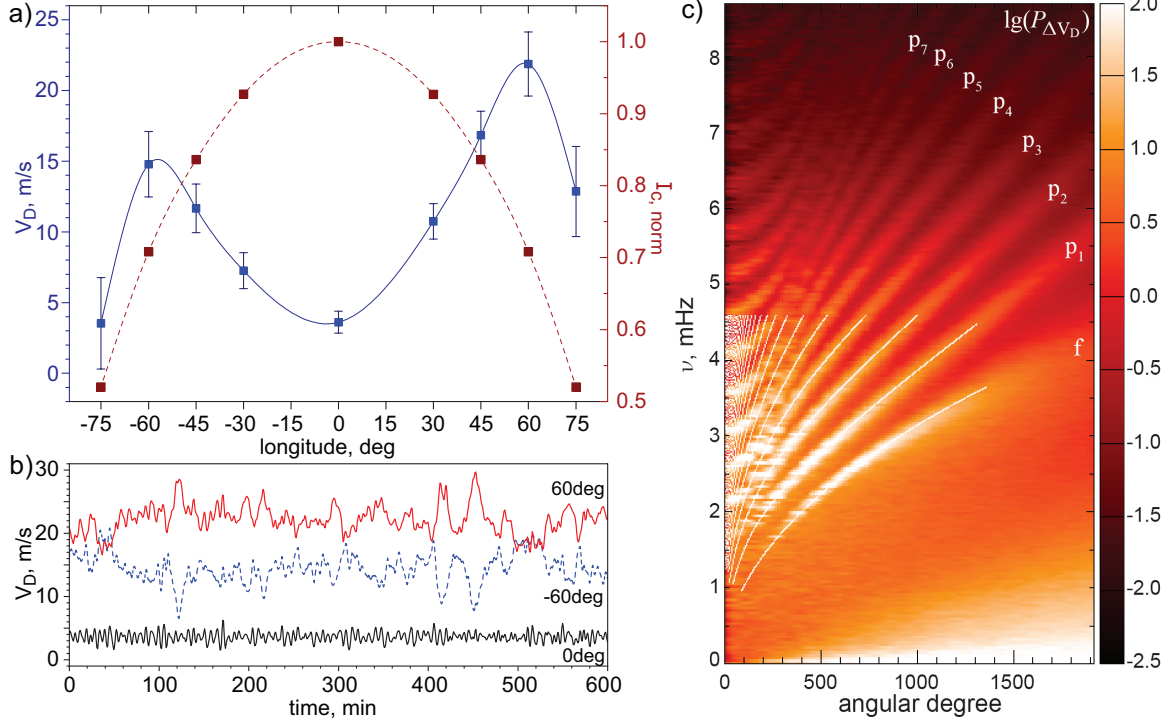


Figure 1. Panel a) Variations with longitude of the Doppler velocity (V_D ; blue curve) and the continuum intensity (I_c ; red curve). Panel b): Comparison of the time variations of V_D at $\pm 60^\circ$ longitudes (red solid and blue dashed curves) and the disk center (black curve) shows 5-minute variations, contribution of the solar rotation, and dynamics of the atmosphere for areas closer to the solar limb. Panel c): The logarithm of the oscillation power spectrum (the ℓ - ν diagram) from synthetic Doppler velocity at the disc center overplotted with the f - and p -modes (white curves) fitted to the observed power spectra from SDO/HMI by (Reiter et al. 2020). The vertical bars in panel a) correspond to 1σ variations for the time difference of V_D .

lanes (Kitiashvili et al. 2011). The surface gravity modes in the observed frequency range are confined in shallow near-surface layers. In contrast to the resonance modes, the pseudo-modes are not trapped inside the Sun. They result from the interference of high-frequency wavefronts that propagate directly from the subsurface acoustic sources and are reflected back into the atmosphere from layers deeper than the source location (Kumar et al. 1990; Nigam & Kosovichev 1999). Transition from the resonance to pseudo-modes determined by the cut-off frequency defined as (Deubner & Gough 1984)

$$\omega_c = \frac{c_s(r)}{2H} \sqrt{1 - 2 \frac{dH}{dr}}, \quad H = \left| \frac{d \log \rho(r)}{dr} \right|^{-1}, \quad (2)$$

where c_s is sound speed, H is the density scale height, ρ is plasma density, and r is the solar radius.

3. GENERAL PROPERTIES OF OBSERVABLES AT DIFFERENT LONGITUDES

The initial overview of the synthesized observables shows a decrease in the mean continuum intensity with increasing distance from the disk center (red squares, Figure 1a), known as the limb darkening effect. The mean of the Doppler velocity increases from the disk center to 60° (blue squares, Figure 1a) and shows a significant decrease for 75° longitude. Because of rotation, the Doppler velocity profile exhibits East–West asymmetry, with faster flows closer to the western limb of the Sun and a more significant velocity decrease at -75° longitude, near the eastern limb. Since we are considering an idealized situation with dynamics identical at all longitudes and the only difference being the viewing angle within the computational domain, the mean variations in Doppler velocity are mostly anticorrelated for opposite viewing angles (Figure 1b). The stronger fluctuations in the flows at greater distances from the disk center reflect a greater contribution from atmospheric dynamics. To remove general systematic changes in the continuum intensity and Doppler velocities, we subtracted the mean values from the corresponding time series for the following analysis. Comparison of the angular degree – frequency ($\ell - \nu$) diagram obtained for the 24-hour Doppler velocity data at the disc center and results of the ridge fitting using the full-disk SDO/HMI Dopplergrams obtained by Reiter et al. (2020) shows a very good alignment of the f - and the first six p -modes (Figure 1c). Because of the limited box size, the ridges for low angular degree ℓ show a saturation for the corresponding frequencies that diverge from observations. We analyze only the fully resolved higher-degree oscillation modes in the simulations.

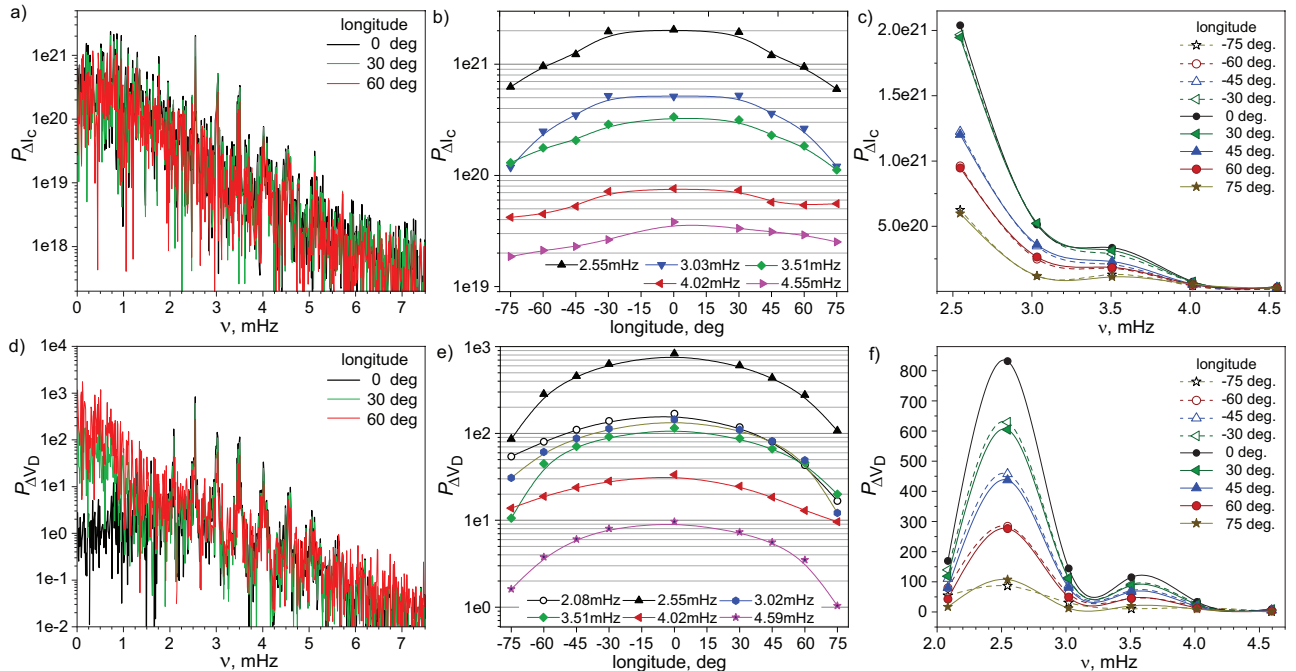


Figure 2. Center to limb variations in the power spectra of the continuum intensity (panel a) and the Doppler velocity (panel b), and the oscillation power changes for five resonance modes for the continuum intensity spectrum (panel c) and six modes from the Doppler velocity spectrum (panel d).

Due to the changes in the properties of the continuum intensity and Doppler velocity with longitude, variations in oscillation properties are expected. In particular, for the continuum intensity (Figure 2a), the power of the spectra decreases for larger distances from the central meridian due to line formation in higher atmospheric layers (e.g., Faurobert et al. 2012; Holzreuter & Solanki 2013; Kitiashvili et al. 2015; Waidele et al. 2023). A more detailed analysis of the power in the continuum intensity carried by each of the five resonance modes shows not only a decrease in power with increasing distance from the disk center, but also the East-West asymmetry in the power distribution (Figure 2b) due to the solar rotation. The asymmetry is becoming stronger at higher frequencies. Interesting to note that the apparent amplitudes of lower-frequency modes (2.55 to 3.51 mHz) are greater when they are observed closer to the East limb than closer to the West limb, whereas the modes at 4.02 and 4.55 mHz show the opposite trend (Figure 2c). These trends are not valid for $\pm 75^\circ$ longitudes (Figure 2c), which can be explained by a very high noise level combined with a significant foreshortening.

In the case of the Doppler velocity (Figure 2d), the power increases closer to the limb. The strongest center-to-limb dependence is observed at both low (below 2 mHz) and high (above 5 mHz) frequencies. As expected, the amplitude of each mode observed in the Doppler velocity decreases more rapidly closer to the limb compared to the modes observed in the continuum intensity power spectra. Also, the effect of the rotation in the Doppler velocity data is more pronounced in the East-West energy distribution for each resonance mode (Figure 2e) in comparison to the continuum intensity. For the six identified modes, the higher amplitude corresponds to areas closer to the East limb. Similar to the continuum intensity, the oscillation power for 75° longitude (near West limb) is higher for 2.55 mHz and 3.51 mHz modes in comparison to the -75° longitude (panel f).

To quantify the oscillatory properties in more detail, we consider the power maps obtained by integrating the oscillation power in eight 1 mHz frequency ranges, from 0.5 mHz to 8.5 mHz (Figure 3). For the continuum intensity, the oscillation power decreases with increasing distance from the disk center at higher frequencies. Also, above the cutoff frequencies (~ 5 mHz), the decrease rate is noticeably smaller at the disk center (black diamonds, Figure 3a). This effect weakens as the distance from the disk center increases. For the power maps computed from the Doppler velocity (Figure 3b), the mean power decreases with the oscillation frequency and for a given frequency increases closer to the limb. At the disc center, the oscillation power shows a slight decrease at low frequencies (below 3.5 mHz) and a faster decrease at higher frequencies. In off-center-of-disc observations, the oscillation power decreases monotonically with increasing frequency.

4. LONGITUDINAL DEPENDENCE OF ACOUSTIC AND SURFACE GRAVITY MODES

Another way to assess the influence of the center-to-limb effect on the observed properties of solar oscillations is to analyze data in the form of azimuthally averaged 3D spectra. These spectra ($\ell - \nu$ diagrams) represent the oscillation power distribution as a function of the angular degree (ℓ) and frequency (ν). The diagrams show the oscillation power carried out by turbulent convective motions (background convective noise), surface gravity (f) and acoustic (p) resonance modes, as well as the pseudo-modes (interference peaks above the acoustic cutoff frequency), the observed properties of which vary with longitude (Figures 1c, 4). To enhance the signal from the resonant and pseudo-modes

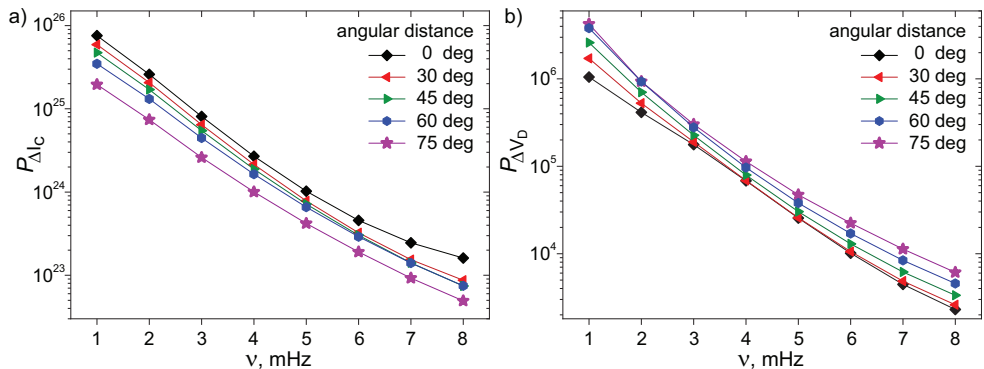


Figure 3. Variations of the acoustic power as a function of the frequency at different distances from the disc center for the continuum intensity (panel a) and the Doppler velocity (panel b). The resulting power from a series of 17 power maps covering eight frequency ranges from 0.5 to 8.5 mHz. Each power map is computed for 1 mHz frequency ranges.

(displayed as ridges above the cutoff frequency), we computed the time difference between snapshots for the time series of continuum intensity and Doppler velocity, then subtracted the mean. Also, 24-hour-long time series have been organized into 8-hour-long subsets, shifted by 1 hour. Figure 4 and the following analysis are based on the averaged diagrams. The center-to-limb effect affects the observational properties of the modes and the background noise differently for the continuum intensity (panel a) and Doppler velocity (panel b). This is related to the non-linear nature of radiative hydrodynamics in a highly stratified medium, with each observable, as well as projection and foreshortening effects, closer to the limb.

4.1. Continuum intensity

The center-to-limb effect in the $\ell - \nu$ diagrams for the continuum intensity (Figure 4a) is manifested as a power decrease for the low-frequency convective noise, all resolved modes, and an enhancement in modes contrast obtained from the data corresponding to observations closer to the solar limb. These effects are linked to changes in the viewing angle, which cause integration through thicker atmospheric layers and increase the foreshortening, leading to the observation of the continuum intensity at higher altitudes in the solar atmosphere. Given that the amplitude of the low-frequency noise associated with photospheric temperature fluctuations decreases rapidly with height, at larger distances from the disc center, a reduction in the background noise allows tracking the oscillation modes up to 75° longitude (Figures 4a and 5a). This effect is particularly evident for pseudo-modes: in the $\ell - \nu$ diagrams constructed for off-disk-center locations, the pseudo-mode signal appears enhanced primarily due to a reduction in the background

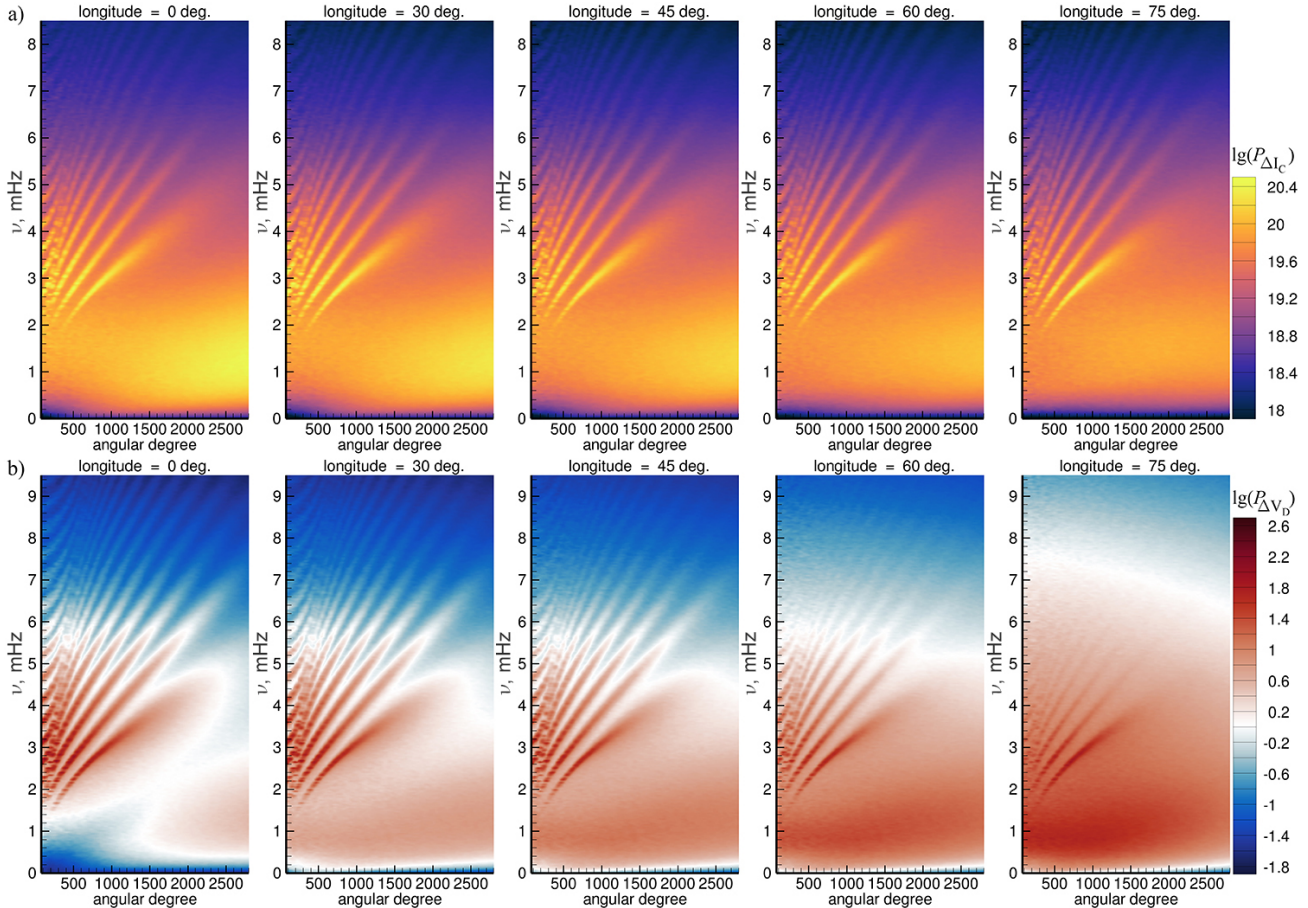


Figure 4. The power spectra distribution as a function of the angular degree and frequency (the $\ell - \nu$ diagrams) obtained for the continuum intensity (panel a) and Doppler velocity fluctuations (panel b) at different distances from the disk center. The presented diagrams are the result of averaging 17 diagrams from an 8-hour time series with a 1-hour time shift. The $\ell - \nu$ diagrams are obtained after applying the running time differencing to the 2D time series of the continuum intensity and the Doppler velocity, and subtracting the mean values.

noise level, even though the absolute pseudo-mode power itself decreases. The relative comparison of modes for areas located 60° from the disk center to the East and West limbs shows some deviations (red and blue curves in Figure 5a), which, however, are within a standard deviation (Figure A1a).

The structural changes in the properties of individual modes with longitude can be illustrated using the frequency-longitude diagrams for the selected spherical harmonic degree. Figure 6 shows a power distribution of the continuum intensity as a function of frequency and longitude for angular degrees $\ell = 506, 752$, and 1011 . The resulting diagrams allow us to identify f - and several p -modes, revealing variations in the energy distribution among the modes at different longitudes. In contrast to the data representation in the form of classical $\ell - \nu$ diagrams (Figures 4a), the

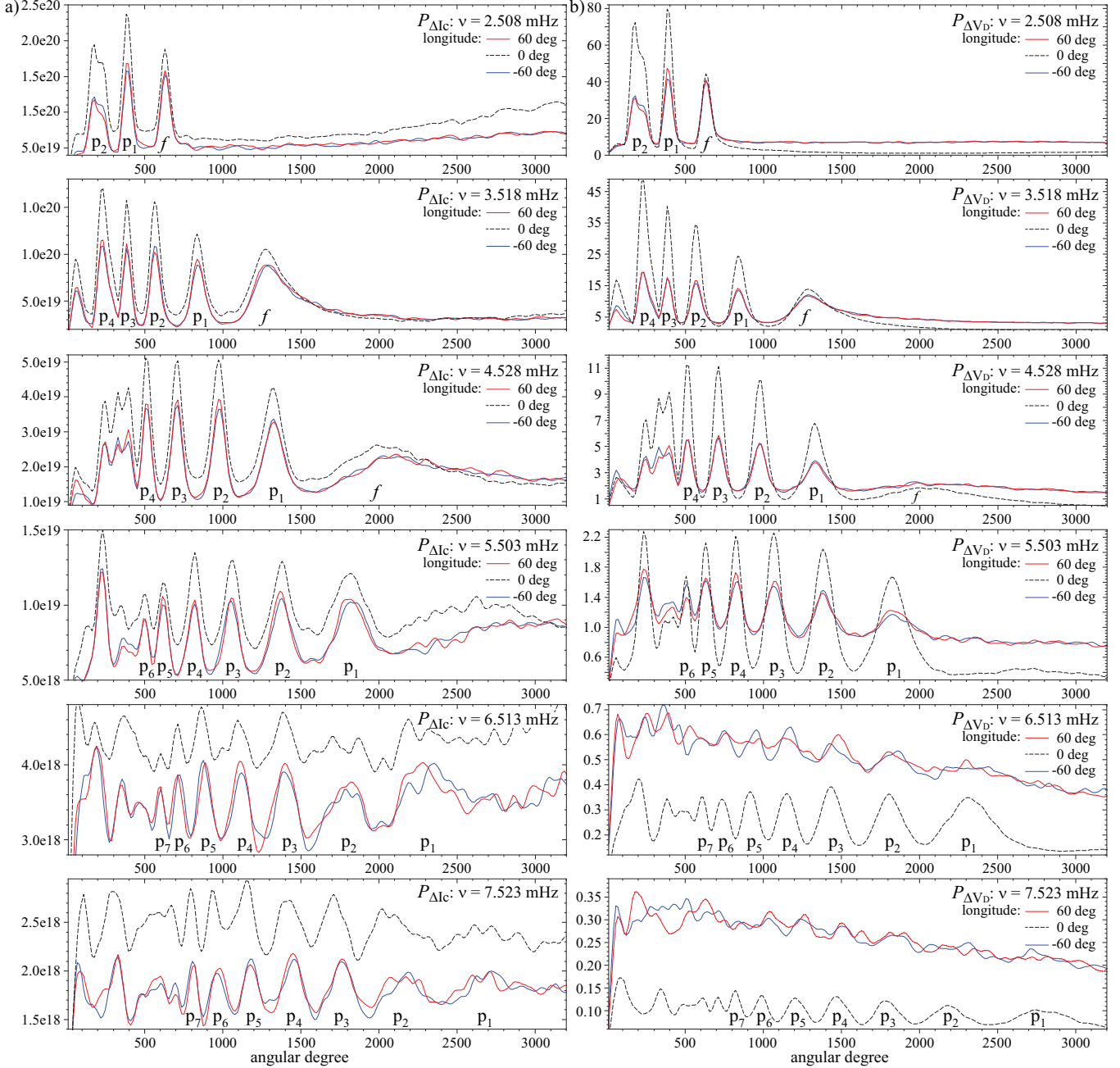


Figure 5. Comparison of the oscillation power for the continuum intensity (panel a) and Doppler velocity (panel b) at $\pm 60^\circ$ longitudes toward the East (blue curves) and West (red curves) limbs at selected frequencies. The plots are extracted from the $\ell - \nu$ diagrams shown in Figure 4. The dashed black curves correspond to the disk center (0°) and are given as a reference.

identification of the high-degree ridges is challenging due to low signal-to-noise and their compact location. In the frequency-longitude diagrams, the signal associated with a particular resonance mode shows the energy enhancements at the disk center (along the horizontal dashed lines in Figure 6), as discussed previously. This property allows us to identify modes up to p_{13} (the radial order, $n = 13$). Nevertheless, it is important to note that the retrieval of information about the properties of modes above p_8 is limited due to a significant weakening of the signal.

Another interesting property revealed by the frequency-longitude diagrams (Figures 6a, c, d) is a decrease in the width of the resonance modes at larger distances from the disk center. The longitudinal variation in the mode width is weaker at lower frequencies. For instance, this effect is more noticeable for high-degree modes (e.g., p_3) than for the f or p_1 modes. Also, the longitudinal variation of the mode width is more pronounced for higher ℓ . The transition from the resonant p modes to the pseudo-modes at about 5 mHz is manifested by a dramatic change in the energy distribution properties (to p_7 for $\ell = 506$; p_5 for $\ell = 752$; to p_4 for $\ell = 1011$; Figures 6a, c, d). At the low frequencies (e.g., for frequencies just below f mode at 2.75 mHz for $\ell = 1011$; Figure 6e), the power distribution reveals the East-West asymmetry that potentially is a result of the radial differential rotation developed in the numerical model (Kitiashvili et al. 2023).

4.2. Doppler velocity

The center-to-limb effect affects the properties of the Doppler velocity oscillations differently from oscillations in the continuum intensity. It manifested as an increase in the background noise at larger distances from the disc center across all frequencies, leading to the weakening and disappearance of higher-degree resonant and pseudo-modes. At the same time, a signal induced by predominantly radial convective motions decreases closer to the limb due to an

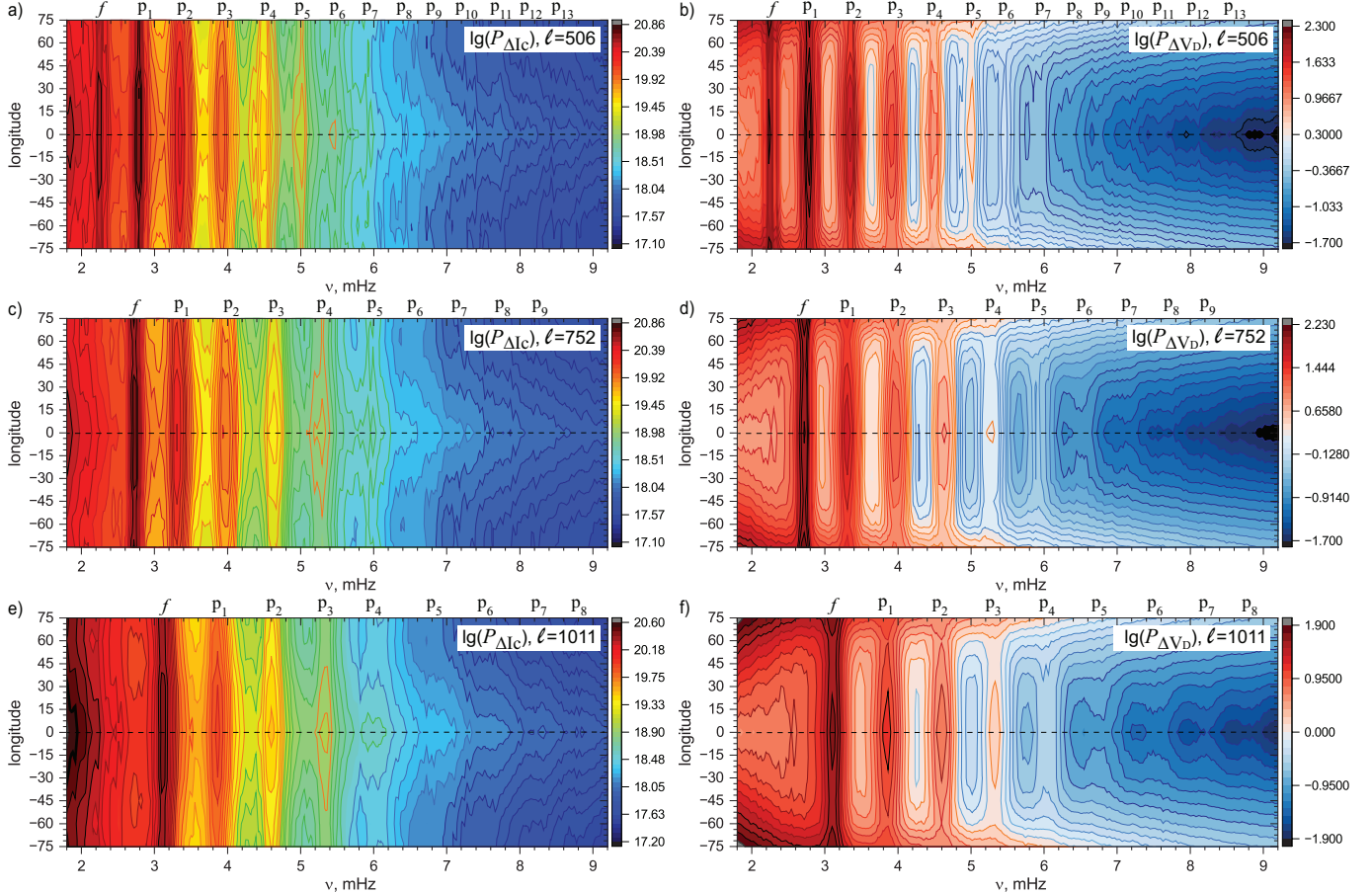


Figure 6. Frequency – longitude diagrams of the oscillation power in the continuum intensity (panels a, c, and e) and the Doppler velocity (panels b, d, and f) obtained for three angular degrees ℓ : 506 (panels a and b), 752 (panels c and d), and 1011 (panels e and f). The numbering of p -modes (p_1, p_2, \dots) indicates the mode radial orders $n = 1, 2, \dots$

increase in the view angle, which causes a significant weakening of f and p modes (Figure 4b). Comparison of the power distribution at the disc center (dashed curves, Figure 5b) and $\pm 60^\circ$ longitudes (red and blue curves), we can note a slower decrease of the power for lower-degree modes (e.g., 3.18 mHz in Figure 5b) and disappearance a distinct signal from the pseudo-modes at the higher frequencies. Comparison of the power of modes at $pm60^\circ$ longitudes didn't show deviations larger than the standard deviation (Figures 4b, A1b). Similar to the continuum intensity, the longitudinal distribution of power of oscillations computed from the Doppler velocities shows a decrease in the mode width closer to the limb, as well as the power reduction (Figures 6b, d, f). However, in contrast to the continuum intensity, there is no significant East–West asymmetry in the power distribution at low frequencies (below the f -mode).

5. IMPACT OF THE CENTER-TO-LIMB EFFECT ON PROPERTIES OF RING-DIAGRAMS

The next step in investigating the center-to-limb effect is to examine the characteristics of 3D spectra derived from continuum intensity and Doppler velocity. To reduce noise and remove background variations, we computed the running time differences and subtracted the mean values from the 2D time series of synthetic observables. The resulting datasets have been split into 8-hour time series with a 1-hour sliding window to compute the 3D spectra. In this section, we consider 3D spectra averaged over the resulting 17 data cubes. To investigate the center-to-limb effect, we consider the ring diagrams that represent 2D slices in the wavevector (k_x, k_y) plane of 3D FFT power spectra (k_x, k_y, ν) for a selected set of frequencies. Each slice shows an energy concentrated in the form of rings (Figure 7). In each ring diagram, the outermost ring corresponds to the surface gravity (f) mode, and the following rings represent pressure (or acoustic, p_1 , p_2 , etc.) modes. The analysis properties of ring diagrams allow the retrieval of information about the structure of subsurface layers (e.g., Schou & Bogart 1998; Howe et al. 2015; Basu & Bogart 2022; Rabello Soares et al. 2024).

5.1. Continuum intensity

In this work, we are evaluating longitudinal variations of ring diagrams for six frequencies from 3 mHz to 5.5 mHz with a step of 0.5 mHz (Figure 7). The center-to-limb effect in the ring diagrams obtained from continuum intensity fluctuations shows a systematic energy redistribution carried by the oscillations and background noise. At the disc center, the energy distribution remains uniform both along the rings, which represent the surface gravity (f) and acoustic (p) modes, and the background. However, even a relatively small shift to the East or West limbs ($\pm 30^\circ$ longitude) results in the power variation within the modes, which causes an excess of power toward the limb and a reduced power in the direction toward the disk center. Note that the power variation is stronger for the outer ring (lower-order mode). These characteristics remain the same from lower to higher frequencies, which causes a significant enhancement of the signal-to-noise ratio at $\pm 60^\circ$ longitudes for p_1 , p_2 , and p_3 pseudo-modes toward the corresponding limb (bottom row in Figure 7). A similar variation is observed in the background noise. Such enhancement for the high frequency oscillations for the near limb observations (e.g., 5.5 mHz, bottom row in Figure 7) can be especially important because it will allow to perform fitting of the rings for observations performed close to the limb and infer the subsurface dynamics of the Sun, whereas utilization the continuum intensity-based ring diagrams at the disk center can be problematic due to the high background noise.

To investigate in more detail how the center-to-limb effect contributes to the power variations in the different directions, we consider the power spectra in the wavevector–frequency diagrams. In the azimuthal plane $(k_x - \nu$, Figure 8), the power distribution shows a systematic low-frequency enhancement toward the East and West limbs and a suppression to the disk center. The asymmetry in the power distribution among the modes shows a significant frequency dependence due to the center-to-limb effect. In particular, at the low frequencies (e.g., $\nu = 2.5$ mHz; Figure A3a), the f -mode power is similar at $\pm 60^\circ$ longitudes (red and blue curves) and the disc center (dashed black curve). The p_1 and p_2 modes are strongly suppressed towards the disk center. It is interesting to note that the f -modes are not sensitive to the center-to limb effect at the low frequencies (e.g., $\nu = 2.5$ mHz in Figure A3a). For the part of the spectrum corresponding to the direction to the disk center ($k_x > 0$ for -60° longitude), the f -mode becomes better pronounced due to the decrease of the background noise (Figures 8, A3a). At the higher frequencies, similar to other modes, the power of the f -mode is suppressed in the part of the spectrum corresponding to direction toward the disk center (Figures 8, A3b). For the meridional plane $(k_y - \nu$, Figure A2), the deviations in the properties toward the equator and the North pole are not apparent and show a systematic energy decrease in the low-frequency background noise and individual ridges for the areas located closer to the East or West limb.

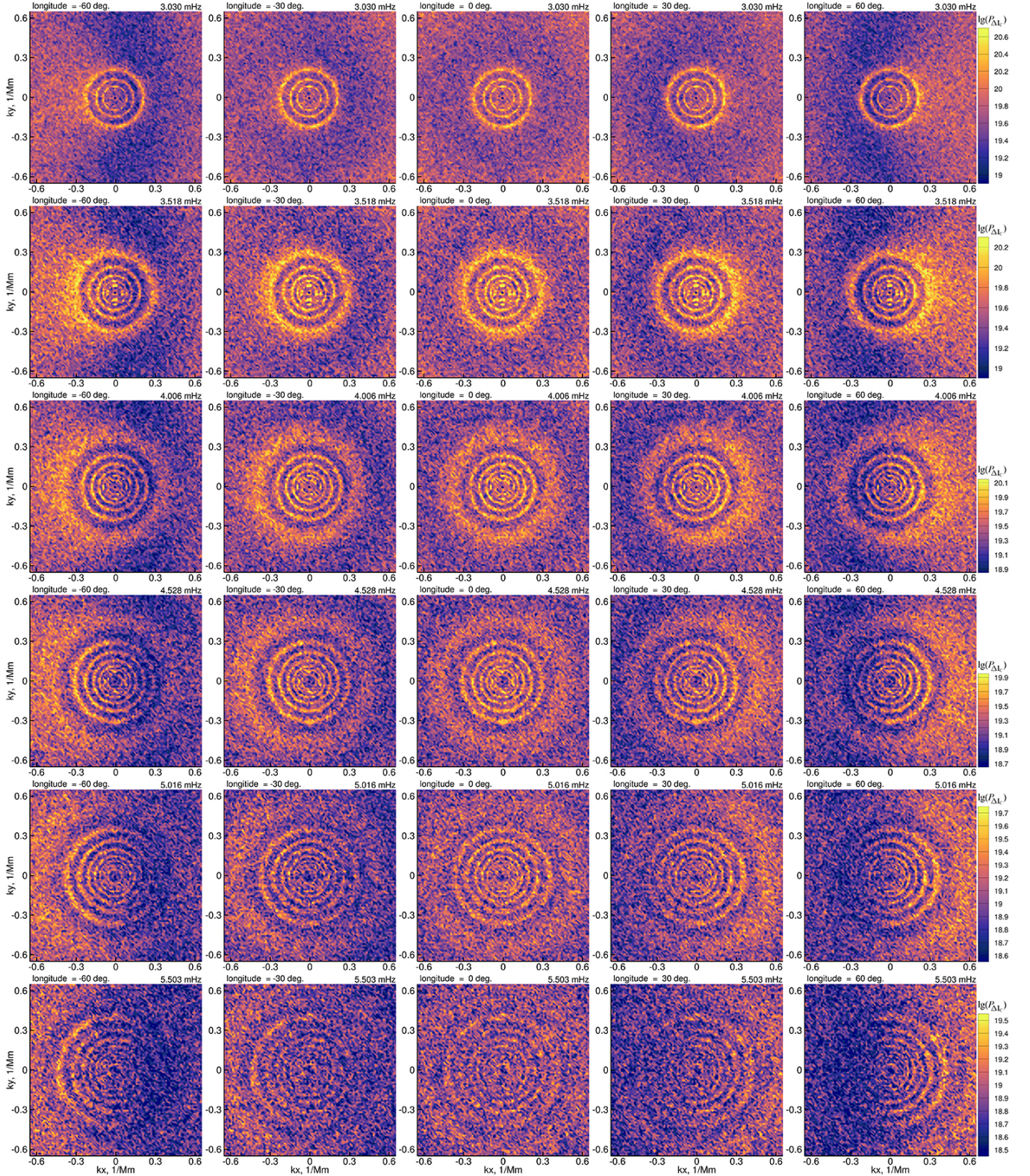


Figure 7. Ring diagrams of the continuum intensity fluctuations at five longitudes (from left to right): -60° , -30° , 0° , 30° , and 60° for five frequencies (from top to bottom): 3.03 mHz, 3.518 mHz, 4.006 mHz, 4.528 mHz, 5.016 mHz, and 5.503 mHz. The ring diagrams are obtained from a 24-hour data set, which is divided into 17 subsets of 8 hours each, with a 1-hour sliding window, and then averaged.

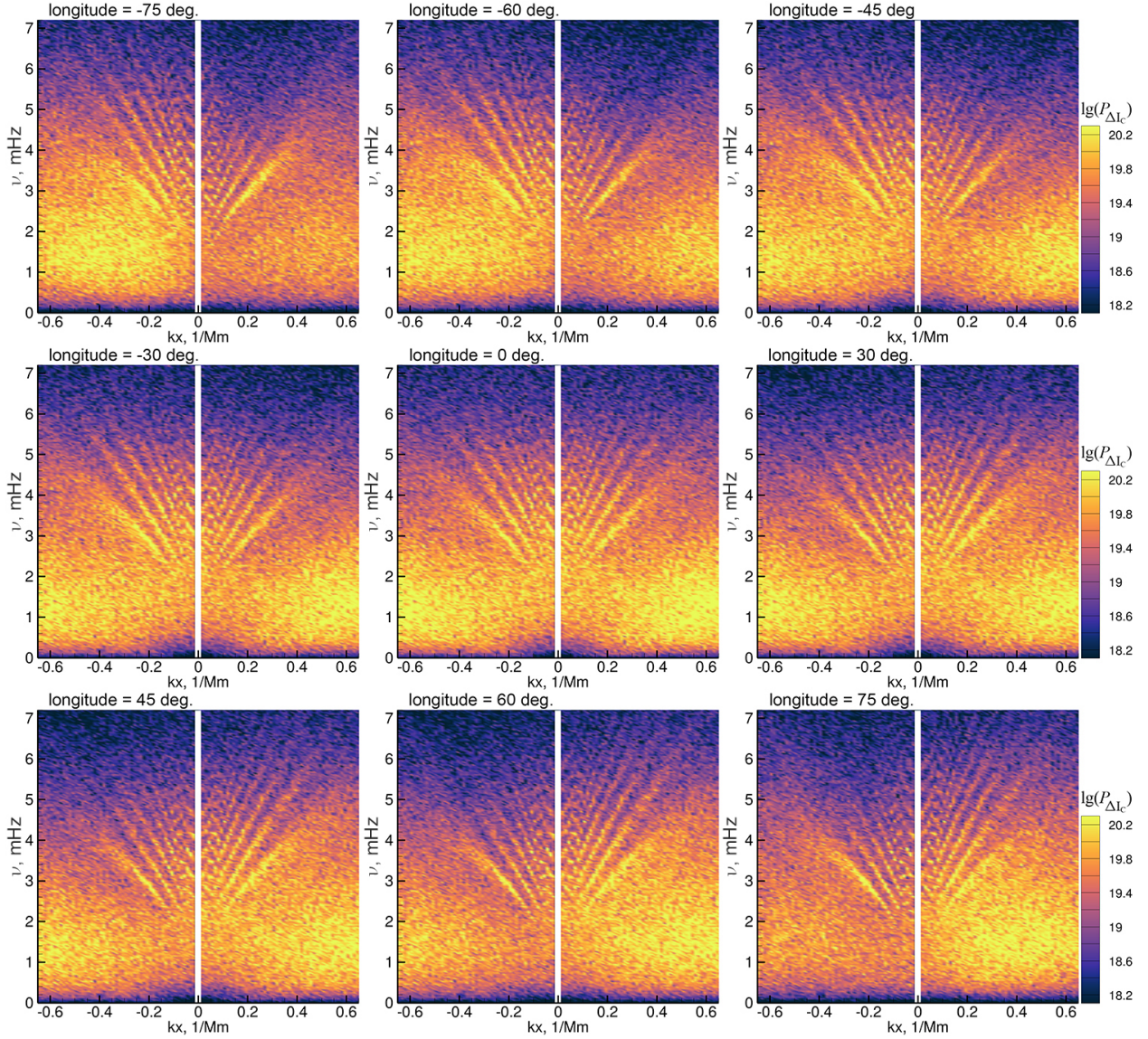


Figure 8. Distribution of the oscillations power in the continuum intensity in the azimuthal plane as a function of the wavenumber (k_x) and frequency (ν) at nine locations on the solar disc from -75° longitude near the East limb to 75° near the West limb.

5.2. Doppler velocity

In the case of the ring diagrams computed from time series of the Doppler velocity fluctuations (Figure 9), at the disc center, the resulting rings have a significantly better contrast in comparison to the continuum intensity. Similar to the continuum intensity-based ring diagrams (Figure 7), the off-disk center data (e.g., $\pm 30^\circ$) show an enhancement of the background noise toward the corresponding limb and the power suppression to the disk center, as well as the similar changes in the power distribution for rings corresponding to the f and p modes (Figure 9). The primary difference is a remarkably clear signal from the modes near the disk center, and a significant reduction closer to the limb due to increased background noise. Interesting to note that the below cut-off frequency at the angular distances of $\pm 60^\circ$ in the direction to the disk center, the ring diagrams show some power enhancement for different modes relative to the pole- or equatorward directions, where power is mostly suppressed.

Similarly to the continuum intensity, we examine how the observed power of solar oscillations is affected by the center-to-limb effect by considering 3D power spectra in the azimuthal plane ($k_x - \nu$; Figure 10) and the meridional plane

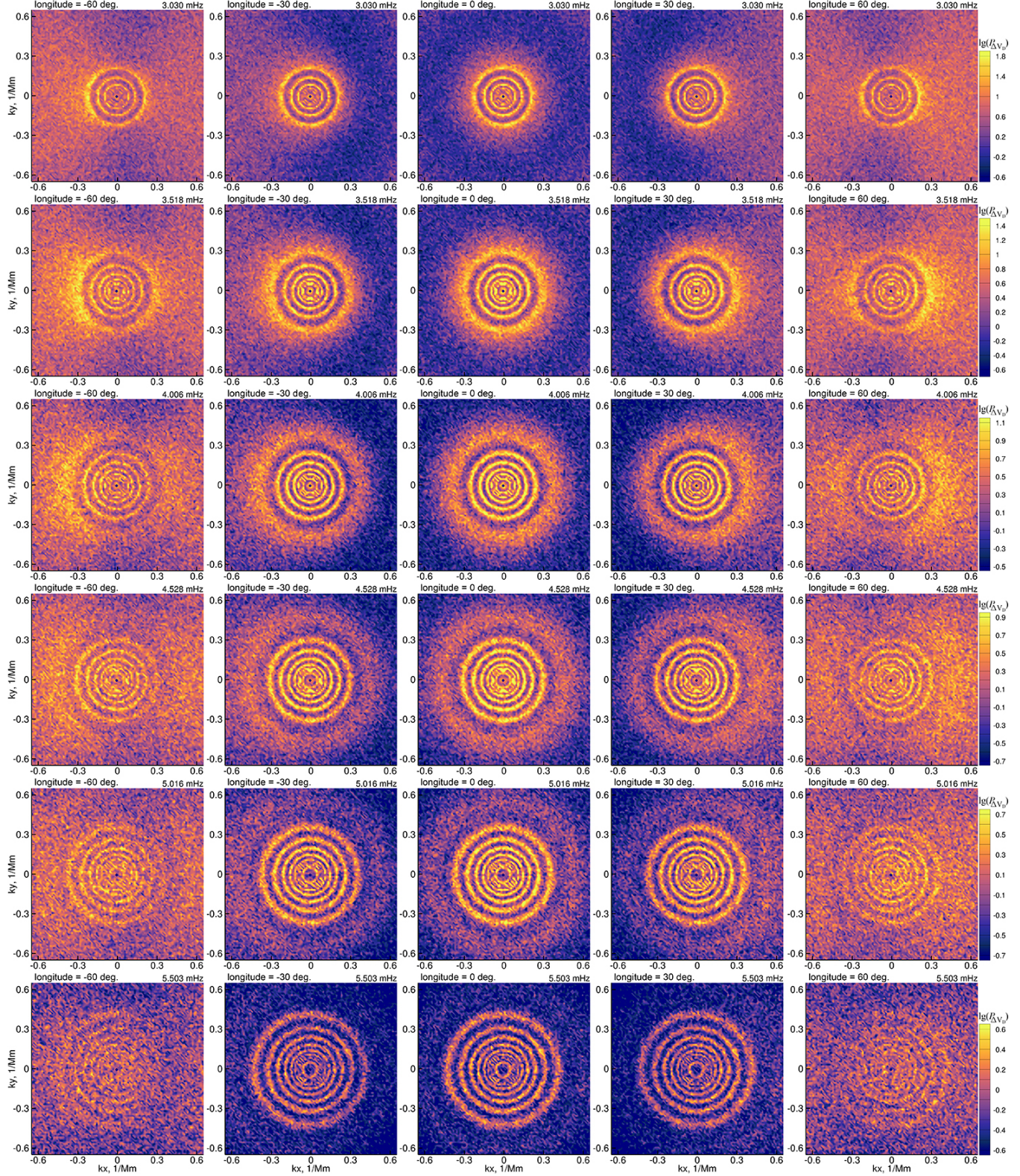


Figure 9. Ring diagrams of the Doppler velocity fluctuations at five longitudes (from left to right): -60° , -30° , 0° , 30° , and 60° for five frequencies (from top to bottom): 3.03 mHz, 3.518 mHz, 4.006 mHz, 4.528 mHz, 5.016 mHz, and 5.503 mHz. The ring diagrams are obtained from a 24-hour data set, which is divided into 17 subsets of 8 hours each, with a 1-hour sliding window, and then averaged.

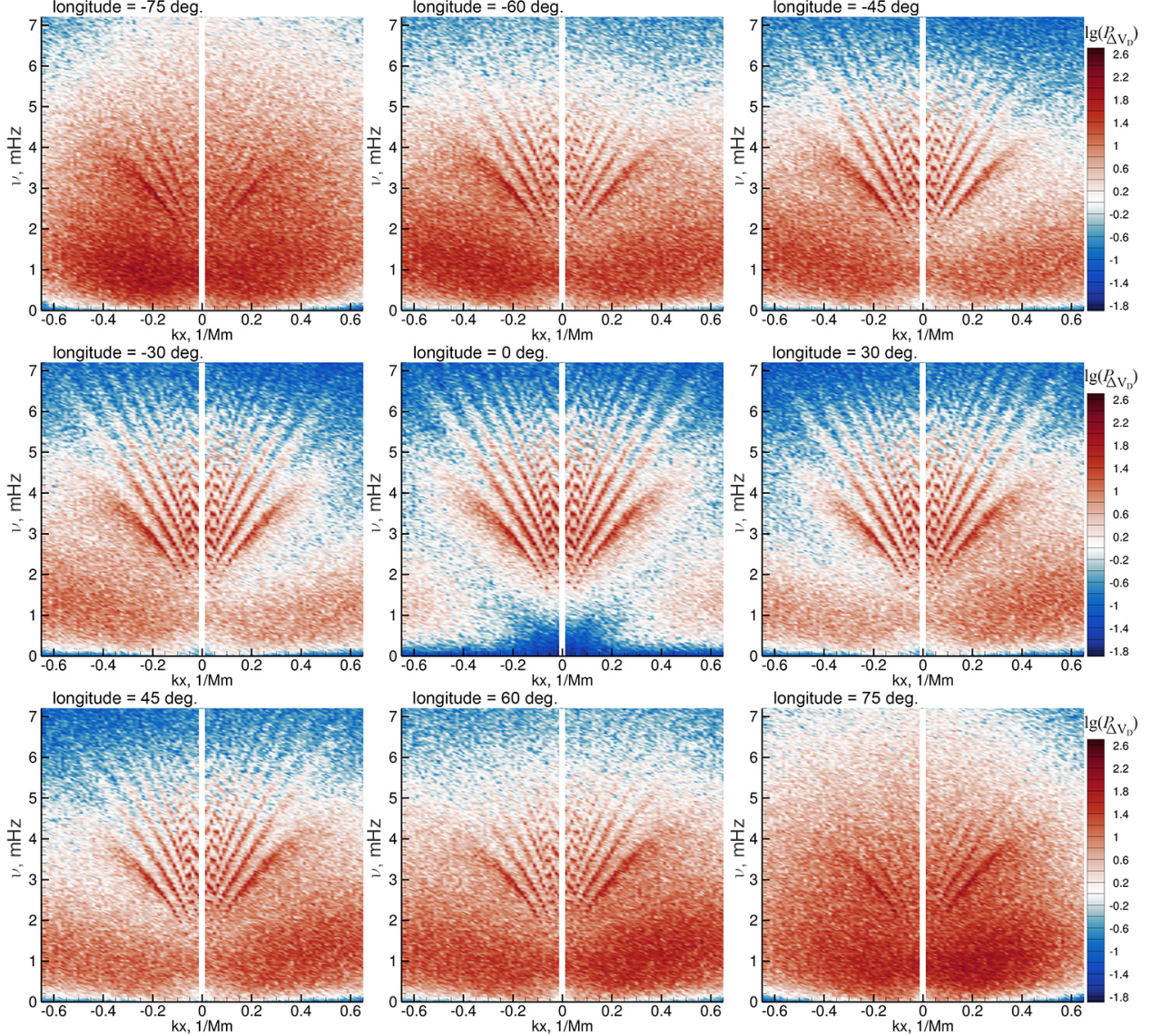


Figure 10. Distribution of the oscillation power for the Doppler velocity oscillations in the azimuthal plane as a function of the wavenumber (k_x) and frequency (ν) at nine locations on the solar disc from -75° longitude near the East limb to 75° near the West limb.

($k_y - \nu$; Figure A4). In the azimuthal plane, the power distribution of the low-frequency noise becomes increasingly asymmetric, with an enhancement toward the limb and a deficit in the opposite direction. Surface gravity and pressure modes show a similar trend in the power distribution and also show the mode extension into the higher frequencies toward the closest limb (Figure 10). The frequency dependence of mode suppression with longitude shows a more homogeneous decrease in power for all modes ($\nu = 2.5$ mHz, Figure A3c). In the case of higher frequencies, the power of the modes shows a systematic variation as a function of the mode degree (e.g., $\nu = 3.5$ mHz, Figure A3d). Also, the pseudo-modes weaken and disappear closer to the limb due to a significant increase in background noise. For the meridional plane ($k_y - \nu$; Figure A4), in general, properties of the background noise and ridges are mostly symmetrical. Similar to the spectra in intensity, some asymmetries are evident in the power distribution of the low-frequency noise and the ridges associated with meridional flows.

6. DISCUSSION AND CONCLUSIONS

To better understand the impact of the center-to-limb effect, we employed 3D radiative hydrodynamic simulations (Kitiashvili et al. 2023), generating 24-hour time series of continuum intensity and Doppler velocity at 9 longitudes spanning -75° to 75° . This setup allows a more direct interpretation of results and links them to observables formed under identical conditions but viewed from different angles, effectively isolating geometric and radiative contributions from intrinsic dynamical effects, and provides a controlled environment to investigate how viewing angle influences the measured solar oscillations and background noise.

The analysis reveals systematic longitudinal variations in both continuum intensity and Doppler velocity power spectra, resulting in a pronounced dependence of the oscillation power on the viewing angle. The overall oscillation power decreases toward the limbs, with a clear asymmetry between the eastern and western hemispheres that becomes stronger at higher frequencies (Figure 2). The integrated oscillation power over a 1 mHz band shows a weakly nonlinear dependence on longitude, with a stronger center-to-limb effect above the acoustic cut-off frequency (Figure 3).

Comparison of the $\ell-\nu$ diagrams derived from both observables shows a consistent reduction in the power of f and p modes and the low-frequency noise with increasing distance from the disk center (Figure 4). However, a different behavior is found for the pseudo-modes: in the continuum intensity, these modes become more pronounced toward the limb, whereas in the Doppler velocity, they are gradually suppressed and merge with the background noise. Analysis of the power distribution with longitude as a function of the frequency for selected angular degrees (ν -longitude diagrams, Figure 6) reveals that the resonance-mode width decreases with increasing distance from the disk center.

The ring diagram spectra further highlight the center-to-limb asymmetry in both observables. The mode power and the background noise are systematically enhanced toward the limb and reduced toward the disk center (Figures 7, 9). Despite their general similarity, three significant differences between the Doppler velocity and the continuum-intensity ring-diagram data are evident. First, the intensity spectra are significantly noisier at the disc center, especially at high frequencies ($\nu \gtrsim 5.5$ mHz), where the rings become indistinct, while Doppler spectra still show clearly defined features. Second, at larger angular distances ($\pm 60^\circ$), the continuum intensity ring-diagrams exhibit asymmetric extensions of the pseudo-mode power toward the limb (Figure 8). The enhancement of the pseudo-modes in the continuum intensity spectra allows for the fitting of rings for corresponding modes even at $\pm 60^\circ$ longitude. In contrast, for the Doppler velocity, the pseudo-modes are best identified at the disk center. In the case of off-disc-center observations, similar to continuum intensity asymmetry, can be noted, but increased noise makes it challenging to identify the modes in the areas close to the limb. This suggests a potential improvement to the ring-diagram analysis for observations obtained closer to the limb by developing an analysis procedure that combines Doppler velocity and continuum intensity observations. Finally, the Doppler velocity-based ring diagrams show a weaker suppression of f -modes toward the disk center for frequencies below 4 mHz that manifested as a slight f -mode enhancement toward the disk center, in addition to a primary increase in the power toward the corresponding limb (Figure 9), whereas in the continuum intensity f -mode shows weaker influence of the center-to-limb effect only for low frequencies (2.5 mHz; Figure A3a) and can give an impression of enhancement due to decrease a level of the background noise that effectively increases contrast. Considering the power distribution for the continuum intensity and the Doppler velocity in the meridional plane ($k_y-\nu$, Figures A2, A4), a weak asymmetry between the equatorward and Northern pole directions can be noted, which may be related to meridional flows (Kitiashvili et al. 2023) and requires a detailed analysis.

These results demonstrate that the center-to-limb effect is not purely geometric, but also depends strongly on the line-formation height and sensitivity of the observable. The Doppler signal, which traces plasma motion, and the continuum intensity, which reflects radiative transfer effects, respond differently to viewing geometry and local flows. The observed asymmetries in mode power, width, and pseudo-mode distribution provide valuable diagnostics for correcting full-disk observations from instruments such as SDO/HMI and Solar Orbiter/PHI, as well as provide an important insight into the more complex coupling of the center-to-limb effect and observed oscillations that require taking into account in improving data analysis techniques and interpretation results. Moreover, this study highlights the potential of realistic 3D radiative hydrodynamic simulations as a powerful framework for disentangling the physical and geometric contributions to systematic observational biases. Future extensions of this work will include the effects of magnetic fields and multiple spectral lines to quantify how magnetic activity and line-formation height influence the center-to-limb behavior of solar oscillations at different latitudes, as well as a more detailed analysis of the radial differential rotation and meridional flows that are already present in models.

ACKNOWLEDGMENTS

Modeling and data analysis of the resulting data have been performed using the NASA Ames Supercomputing Facility. The presented investigation has been supported by the NASA Heliophysics Guest Investigator - Open Program (23-HGIO23_2-0077), and the Science DRIVE (Diversify, Realize, Integrate, Venture, Educate) Center Program (COFFIES Project “Consequences of Fields and Flows in the Interior and Exterior of the Sun”; 80NSSC22M0162).

REFERENCES

Adams, W. S. 1910, *ApJ*, 31, 30, doi: [10.1086/141722](https://doi.org/10.1086/141722)

Basu, S., & Bogart, R. S. 2022, *SoPh*, 297, 101, doi: [10.1007/s11207-022-02034-0](https://doi.org/10.1007/s11207-022-02034-0)

Böning, V. G. A., Birch, A. C., Gizon, L., & Duvall, T. L. 2021, *A&A*, 649, A59, doi: [10.1051/0004-6361/202039311](https://doi.org/10.1051/0004-6361/202039311)

Chen, R., & Zhao, J. 2018, *ApJ*, 853, 161, doi: [10.3847/1538-4357/aaa3e3](https://doi.org/10.3847/1538-4357/aaa3e3)

Christensen-Dalsgaard, J. 2002, *Reviews of Modern Physics*, 74, 1073, doi: [10.1103/RevModPhys.74.1073](https://doi.org/10.1103/RevModPhys.74.1073)

Couvidat, S., Zhao, J., Birch, A. C., et al. 2012, *SoPh*, 275, 357, doi: [10.1007/s11207-010-9652-y](https://doi.org/10.1007/s11207-010-9652-y)

Deubner, F.-L., & Gough, D. 1984, *ARA&A*, 22, 593, doi: [10.1146/annurev.aa.22.090184.003113](https://doi.org/10.1146/annurev.aa.22.090184.003113)

Duvall, T. L., J., & Hanasoge, S. M. 2009, in *Astronomical Society of the Pacific Conference Series*, Vol. 416, *Solar-Stellar Dynamos as Revealed by Helio- and Asteroseismology: GONG 2008/SOHO 21*, ed. M. Dikpati, T. Arentoft, I. González Hernández, C. Lindsey, & F. Hill, 103. <https://arxiv.org/abs/0905.3132>

Evershed, J. 1931, *MNRAS*, 92, 105, doi: [10.1093/mnras/92.2.105](https://doi.org/10.1093/mnras/92.2.105)

—. 1936, *MNRAS*, 96, 152, doi: [10.1093/mnras/96.3.152](https://doi.org/10.1093/mnras/96.3.152)

Faurobert, M., Ricort, G., & Aime, C. 2012, *A&A*, 548, A80, doi: [10.1051/0004-6361/201219640](https://doi.org/10.1051/0004-6361/201219640)

Frutiger, C., Solanki, S. K., Fligge, M., & Bruls, J. H. M. J. 2000, *A&A*, 358, 1109

Georgobiani, D., Zhao, J., Kosovichev, A. G., et al. 2007, *ApJ*, 657, 1157, doi: [10.1086/511148](https://doi.org/10.1086/511148)

Goldreich, P., & Kumar, P. 1988, *ApJ*, 326, 462, doi: [10.1086/166108](https://doi.org/10.1086/166108)

Hathaway, D. H., Upton, L. A., & Mahajan, S. S. 2022, *Frontiers in Astronomy and Space Sciences*, 9, 419, doi: [10.3389/fspas.2022.1007290](https://doi.org/10.3389/fspas.2022.1007290)

Higgs, L. A. 1960, *MNRAS*, 121, 421, doi: [10.1093/mnras/121.5.421](https://doi.org/10.1093/mnras/121.5.421)

Hill, F. 1988, *ApJ*, 333, 996, doi: [10.1086/166807](https://doi.org/10.1086/166807)

Holzreuter, R., & Solanki, S. K. 2013, *A&A*, 558, A20, doi: [10.1051/0004-6361/201322135](https://doi.org/10.1051/0004-6361/201322135)

Howard, R., & Harvey, J. 1970, *SoPh*, 12, 23, doi: [10.1007/BF02276562](https://doi.org/10.1007/BF02276562)

Howe, R. 2020, *Astrophysics and Space Science Proceedings*, 57, 63, doi: [10.1007/978-3-030-55336-4_8](https://doi.org/10.1007/978-3-030-55336-4_8)

Howe, R., Komm, R. W., Baker, D., et al. 2015, *SoPh*, 290, 3137, doi: [10.1007/s11207-015-0747-3](https://doi.org/10.1007/s11207-015-0747-3)

Ilonidis, S., Zhao, J., & Kosovichev, A. 2011, *Science*, 333, 993, doi: [10.1126/science.1206253](https://doi.org/10.1126/science.1206253)

Kasapis, S., Kitashvili, I. N., Kosovichev, A. G., & Stefan, J. T. 2025, *ApJS*, 280, 64, doi: [10.3847/1538-4365/adfbe2](https://doi.org/10.3847/1538-4365/adfbe2)

Kashyap, S. G., & Hanasoge, S. M. 2025, *ApJ*, 978, 78, doi: [10.3847/1538-4357/ad9476](https://doi.org/10.3847/1538-4357/ad9476)

Kitiashvili, I. N., Couvidat, S., & Lagg, A. 2015, *ApJ*, 808, 59, doi: [10.1088/0004-637X/808/1/59](https://doi.org/10.1088/0004-637X/808/1/59)

Kitiashvili, I. N., Kosovichev, A. G., Mansour, N. N., & Wray, A. A. 2011, *ApJL*, 727, L50, doi: [10.1088/2041-8205/727/2/L50](https://doi.org/10.1088/2041-8205/727/2/L50)

Kitiashvili, I. N., Kosovichev, A. G., Mansour, N. N., Wray, A. A., & Sandstrom, T. A. 2019, *ApJ*, 872, 34, doi: [10.3847/1538-4357/aafac1](https://doi.org/10.3847/1538-4357/aafac1)

Kitiashvili, I. N., Kosovichev, A. G., Wray, A. A., Sadykov, V. M., & Guerrero, G. 2023, *MNRAS*, 518, 504, doi: [10.1093/mnras/stac2946](https://doi.org/10.1093/mnras/stac2946)

Komm, R. 2021, *SoPh*, 296, 174, doi: [10.1007/s11207-021-01923-0](https://doi.org/10.1007/s11207-021-01923-0)

Kosovichev, A. G. 2011, in *Lecture Notes in Physics*, Berlin Springer Verlag, ed. J.-P. Rozelot & C. Neiner, Vol. 832, 3, doi: [10.1007/978-3-642-19928-8_1](https://doi.org/10.1007/978-3-642-19928-8_1)

Kosovichev, A. G., & Duvall, T. L. 2006, *SSRv*, 124, 1, doi: [10.1007/s11214-006-9112-z](https://doi.org/10.1007/s11214-006-9112-z)

Kosovichev, A. G., Basu, S., Bekki, Y., et al. 2025, *SoPh*, 300, 70, doi: [10.1007/s11207-025-02480-6](https://doi.org/10.1007/s11207-025-02480-6)

Kumar, P., Duvall, Jr., T. L., Harvey, J. W., et al. 1990, in *Progress of Seismology of the Sun and Stars*, ed. Y. Osaki & H. Shibahashi, Vol. 367, 87, doi: [10.1007/3-540-53091-6_68](https://doi.org/10.1007/3-540-53091-6_68)

Lamb, D. A. 2017, *ApJ*, 836, 10, doi: [10.3847/1538-4357/836/1/10](https://doi.org/10.3847/1538-4357/836/1/10)

Nigam, R., & Kosovichev, A. G. 1999, *ApJL*, 514, L53, doi: [10.1086/311939](https://doi.org/10.1086/311939)

Pesnell, W. D., Thompson, B. J., & Chamberlin, P. C. 2012, *SoPh*, 275, 3, doi: [10.1007/s11207-011-9841-3](https://doi.org/10.1007/s11207-011-9841-3)

Rabello Soares, M. C., Basu, S., & Bogart, R. S. 2024, *ApJ*, 967, 143, doi: [10.3847/1538-4357/ad3d59](https://doi.org/10.3847/1538-4357/ad3d59)

Reiter, J., Rhodes, E. J., J., Kosovichev, A. G., et al. 2020, *ApJ*, 894, 80, doi: [10.3847/1538-4357/ab7a17](https://doi.org/10.3847/1538-4357/ab7a17)

Roudier, T., Švanda, M., Ballot, J., Malherbe, J. M., & Rieutord, M. 2018, *A&A*, 611, A92, doi: [10.1051/0004-6361/201732014](https://doi.org/10.1051/0004-6361/201732014)

Scherrer, P. H., Schou, J., Bush, R. I., et al. 2012, *SoPh*, 275, 207, doi: [10.1007/s11207-011-9834-2](https://doi.org/10.1007/s11207-011-9834-2)

Schou, J., & Bogart, R. S. 1998, *ApJL*, 504, L131, doi: [10.1086/311575](https://doi.org/10.1086/311575)

Stefan, J. T., & Kosovichev, A. G. 2022, *ApJ*, 930, 10, doi: [10.3847/1538-4357/ac602a](https://doi.org/10.3847/1538-4357/ac602a)

—. 2023, *ApJ*, 948, 1, doi: [10.3847/1538-4357/acc836](https://doi.org/10.3847/1538-4357/acc836)

Stefan, J. T., Kosovichev, A. G., Guerrero, G., & Stejko, A. M. 2025, arXiv e-prints, arXiv:2505.05454, doi: [10.48550/arXiv.2505.05454](https://doi.org/10.48550/arXiv.2505.05454)

Stein, R. F. 1967, *SoPh*, 2, 385, doi: [10.1007/BF00146490](https://doi.org/10.1007/BF00146490)

Stejko, A. M., Kosovichev, A. G., Featherstone, N. A., et al. 2022, *ApJ*, 934, 161, doi: [10.3847/1538-4357/ac7a44](https://doi.org/10.3847/1538-4357/ac7a44)

Stejko, A. M., Kosovichev, A. G., & Mansour, N. N. 2021, *ApJS*, 253, 9, doi: [10.3847/1538-4365/abd3fe](https://doi.org/10.3847/1538-4365/abd3fe)

Stenflo, J. O. 2015, *A&A*, 573, A74, doi: [10.1051/0004-6361/201424685](https://doi.org/10.1051/0004-6361/201424685)

Ulrich, R. K., Tran, T., & Boyden, J. E. 2023, *SoPh*, 298, 123, doi: [10.1007/s11207-023-02215-5](https://doi.org/10.1007/s11207-023-02215-5)

Unno, W., & Kato, S. 1962, *PASJ*, 14, 417, doi: [10.1093/pasj/14.4.417](https://doi.org/10.1093/pasj/14.4.417)

Waidele, M., Zhao, J., & Kitiashvili, I. N. 2023, *ApJ*, 949, 99, doi: [10.3847/1538-4357/accae2](https://doi.org/10.3847/1538-4357/accae2)

Wray, A. A., Bensassiy, K., Kitiashvili, I. N., Mansour, N. N., & Kosovichev, A. G. 2018, *Realistic Simulations of Stellar Radiative MHD*, ed. J. P. Rozelot & E. S. Babayev, 39

Zhao, J., Georgobiani, D., Kosovichev, A. G., et al. 2007, *ApJ*, 659, 848, doi: [10.1086/512009](https://doi.org/10.1086/512009)

Zhao, J., Kosovichev, A. G., & Sekii, T. 2010, *ApJ*, 708, 304, doi: [10.1088/0004-637X/708/1/304](https://doi.org/10.1088/0004-637X/708/1/304)

Zhao, J., Nagashima, K., Bogart, R. S., Kosovichev, A. G., & Duvall, T. L., J. 2012, *ApJL*, 749, L5, doi: [10.1088/2041-8205/749/1/L5](https://doi.org/10.1088/2041-8205/749/1/L5)

Zhao, J., Stejko, A., & Chen, R. 2016, *SoPh*, 291, 731, doi: [10.1007/s11207-016-0864-7](https://doi.org/10.1007/s11207-016-0864-7)

APPENDIX A

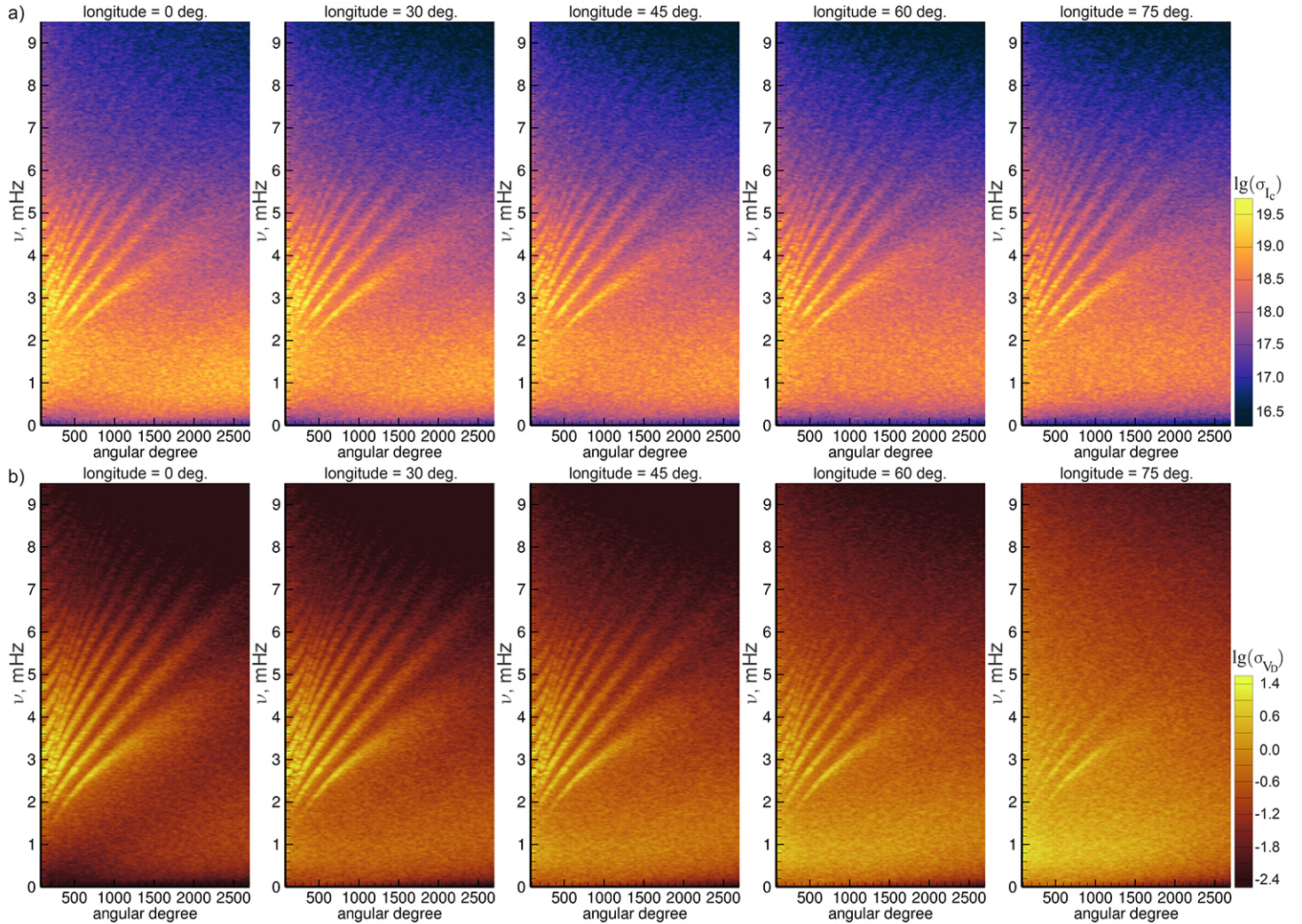


Figure A1. Distribution of the standard deviation as a function of the angular degree and frequency for the power in the continuum intensity (panel a) and the Doppler velocity (panel b) at different longitudes from the disk center (left-most panel) to 75° longitude near the West limb.

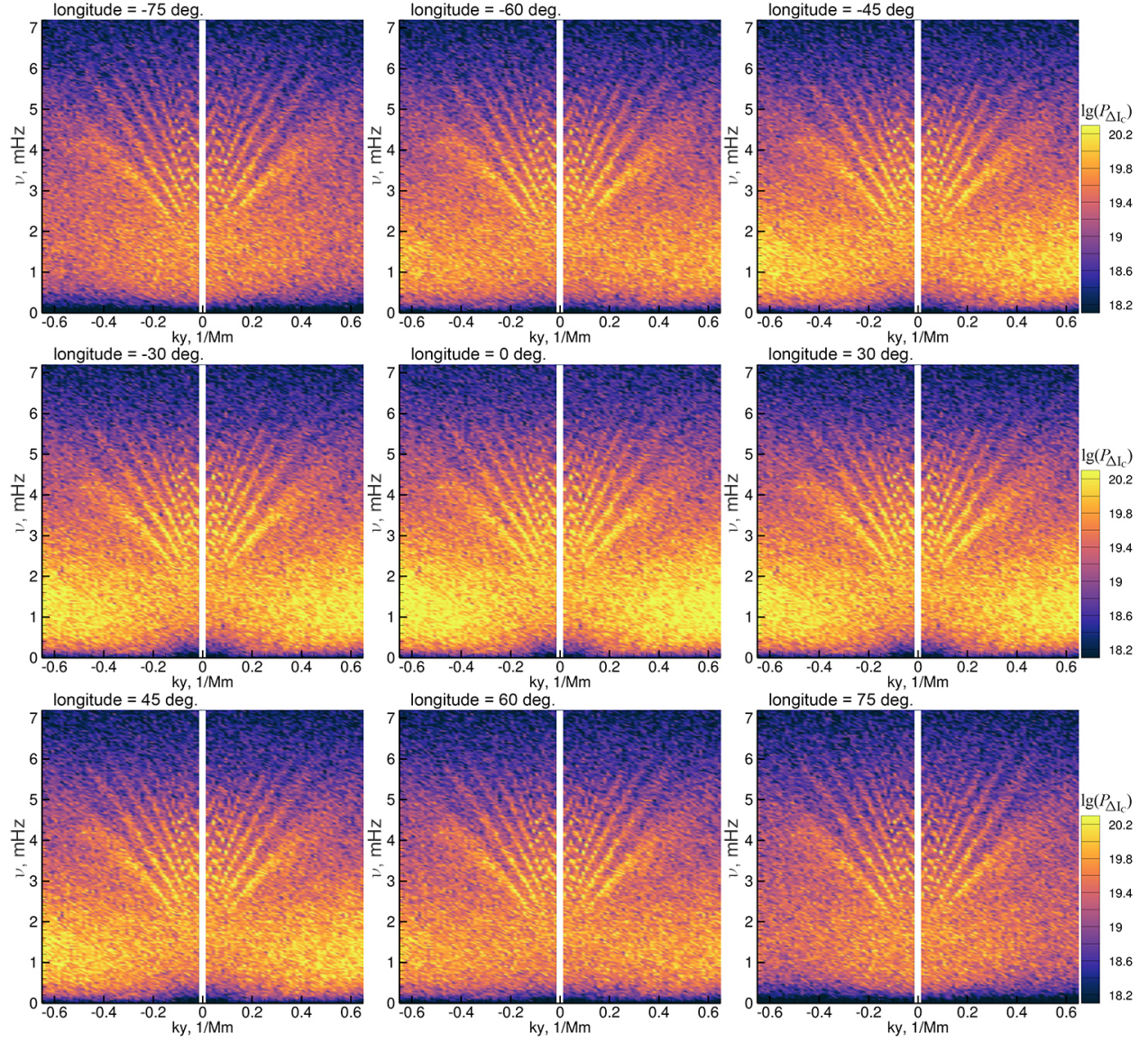


Figure A2. Distribution of oscillations in the continuum intensity in the meridional plane as a function of the wavenumber (k_y) and frequency (ν) at nine locations on the solar disc from -75° longitude near the East limb to 75° near the West limb.

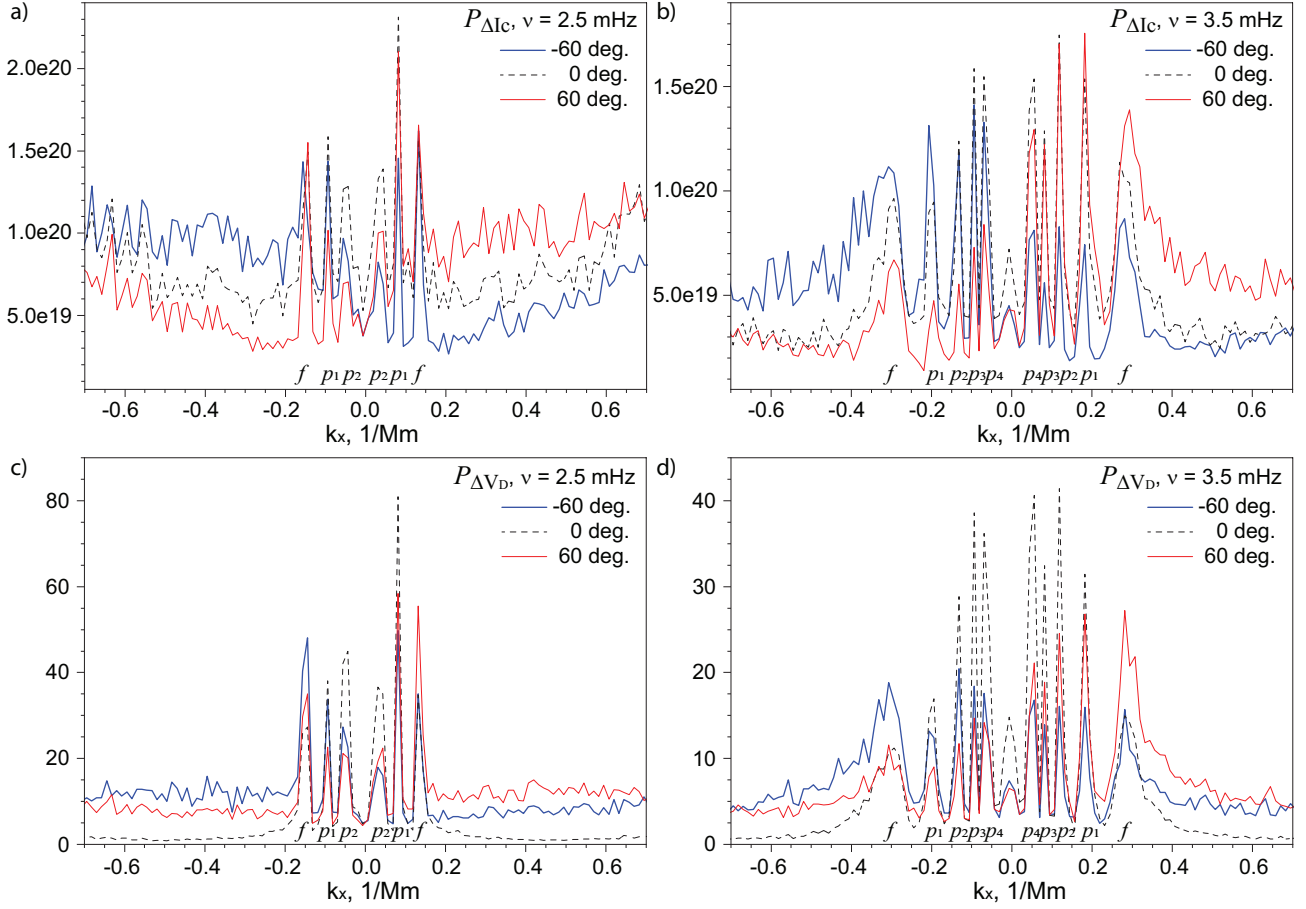


Figure A3. The power distribution in the intensity continuum (panel a, b) and Doppler velocity fluctuations in the azimuthal plane for 2.5 mHz (left panels) and 3.5 mHz (right) for three longitudes: -60° (blue curves, near East limb), 0° (black dashed curves, disc center), and 60° (red curves, near West limb). The power spectra have been extracted from the 3D power spectra from Figures 7 and 9. To reduce noise, each power spectrum was averaged over 0.1 mHz around the indicated frequency, and over the wavenumber $\Delta k_y = 0.05 \text{ 1/Mm}$.

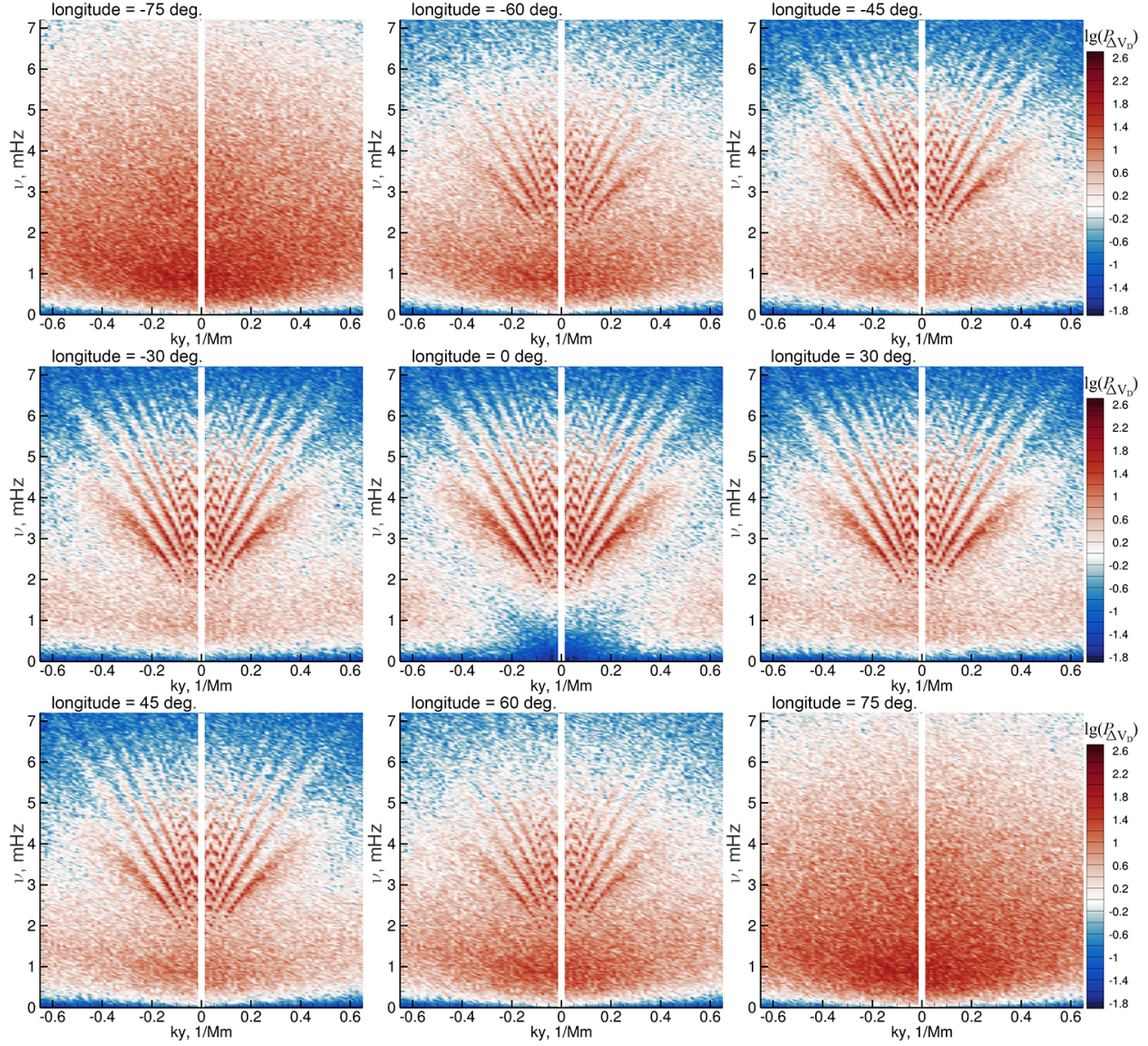


Figure A4. Distribution of oscillation power in the Doppler velocity in the meridional plane as a function of the wavenumber (k_y) and frequency (ν) at nine locations on the solar disc from -75° longitude near the East limb to 75° near the West limb.